



Additive manufacturing process design for complex aircraft components

Ramona Dogea¹ · Xiu T. Yan¹ · Richard Millar²

Received: 15 July 2022 / Accepted: 30 October 2022
© The Author(s) 2022

Abstract

The process of metal additive manufacturing (AM) is now widely used in fabricating complex parts in today's industry. The scope of this paper is to redesign a manufacturing process for complex aircraft components using wing ribs as example by considering embedded Internet of Things (IoT) sensory capability that can be used in an Industry 4.0 ecosystem for moving away from a condition-based preventive maintenance system to a data-driven predictive maintenance-based system. This work is based on a previous study that considered the part design stage which deals with finding the best design solution for a single part. Considering a wing rib geometry of 3-mm web thickness with 6-mm upper and lower caps, the manufacturing process is designed and assessed using the Simufact Additive™ software. The use of AM when embedding IoT sensors allows more flexibility without compromising the structural integrity of parts, as well as the advantage of design freedom and limited cost when modifying geometries. The outcomes show that the manufacturing process depends strongly on hot isostatic pressing (HIP) for the wing rib, but for the sensory covers it presented no significant improvement. The results also show that the support optimisation can lead to an important reduction of mass and volume as well as an improvement of the structural performance.

Keywords Aircraft wing rib · AM · Metal powder bed fusion · Simufact Additive™ · IoT · Predictive maintenance

1 Introduction

Certain aspects of the metal additive manufacturing (AM) processes depend to some extent or other on the use of a heat source. This can be in the form of an electron beam, a laser or an arc or it can even depend on the process of raw material supply. There are two approaches to AM, specifically the powder bed fusion (PBF) and direct energy deposition (DED) processes, that can be used for manufacturing metal parts with no requirements for a secondary casting or infiltration process. Both processes can be used for manufacturing metal components with near-full density [1]. PBF generates a three-dimensional part by means of a layer-by-layer laser fusion of metallic powders [2] and can be split into two sub-processes, where these are defined principally by the source of fusion, by the use of either an electron beam or a laser [3].

Electron beam powder bed fusion (EBPBF) uses a high energy electron beam to melt sequential layers of a metal powder to lead to the manufacture of solid components of the required density. This category of part has to be fabricated in a vacuum due to the physical requirements of the electron beam. AM systems of the sort just described usually require a larger feedstock powder size, and this results in higher surface roughness. The AM build time is, however, generally lower because of the use of high power and rapid scanning for the electron beam [4, 5]. Another AM process is termed laser powder bed fusion (LPBF) and this is increasingly common in industry, thanks to its capability for high resolution and high-quality part production. LPBF employs at least one high power laser to melt and solidify the layers of powdered metal. This procedure is based on a powder feedstock delivered to and then coated on a platform, at which point the powder is melted and solidified in a precise manner under the control of a computer-aided design (CAD) model. Key parameters, such as laser power and layer thickness in particular, are user controllable for a particular material and application.

DED technologies operate in a different manner to PBF, requiring local deposition of the material stock through the use of a powder or wire-feed directly into the melt pool, noting that this can be initiated by a high energy in the form of a controlled electric

✉ Ramona Dogea
ramona.dogea@strath.ac.uk

¹ Department of Design, Manufacture and Engineering Management (DMEM), University of Strathclyde, Glasgow, Scotland

² National Manufacturing Institute Scotland, University of Strathclyde, Glasgow, Scotland

arc, a suitable laser or a high energy electron beam. DED can be used to manufacture very large components because it does not need a powder bed. It should be clarified that DED generally produces components at lower resolution compared to those obtainable from powder bed-based technologies [4]. AM in general is now popular within the aerospace industry for the production of critically important metallic parts [6] due to the inherently reduced lead time and costs, and also the fact that complex lightweight geometries of high performance can be reliably produced through these manufacturing technologies. AM offers an inherently high-speed capability for the manufacture of replacement parts, and can be significantly faster than other manufacturing processes, with excellent resources available for localised heat treatment, surface hardening and alloying, the precision removal of material, repairs and high-performance prototyping [7]. In addition to this, AM provides the designer with options for integrated lightweight design, and a consequential reduction in the number of system components [8]. Processes of metal AM are inherently different to the more conventional subtractive machining, using feedstocks of some form to build the component up in a layer-by-layer manner, and employ powders or wires melted or fused by heat sources. These materials are then solidified to generate the required geometry on the basis of a heat source path that can be defined within a digital process [9]. AM capabilities can be optimised for specific applications and such processes are now standardised within ISO/ASTM 52,900 [10]. We note that PBF is the principal technique for the production of metallic parts [11]. Current research shows that the AM part orientation has a big influence on the properties of the final part and the amount of the support structure needed. Furthermore, the selected part orientation affects the support contact area, surface roughness and build time, as well as the cost of the manufactured parts [12]. Support structures can be perceived as a waste in the AM process since they consume powder and energy [13], and the build time is increased as well as the cost of the part due to the additional material and the removal process [14]. The support structures should be analysed by a draft angle and potentially modified to minimise the amount of material and manufacturing costs involved [15]. The main purpose of creating support structures is to assist printability in the manufacturing process. A 3D model with different geometries with holes or edge features, for example, will need a support structure for a successful fabrication since the support structure is necessary to keep the printed parts in the desired position.

In the aerospace industry, the most appropriate process for fabricating aluminium parts is the selective laser melting (SLM), a layer-by-layer process, which will be involved at this process design stage. The fabrication of smart structures using the AM technique can allow the flexibility of embedding sensors within a structure without compromising the structure and/or its functionality. Conversely, using traditional manufacturing by placing sensors increases the possibility of disturbing the normal operation of systems due to the sensor placement design [16]. There are two parameters that have most attention in current studies: laser power and scan/laser

speed. In [17], a matrix of power and speed settings was created in order to understand the relationship between power and speed for metal powder bed fusion processes. They varied power from 50 to 200 W and speed from 100 to 250 mm/s. For stainless steel, the optimum weld bead was found between 150 and 200 W and 175 and 225 mm/s. Wang et al. investigated the effect of power and speed machine in SLM of aluminium and its alloys. The laser scan speed was varied from 1455 to 182 mm/s, whilst the laser power was reduced from an optimum value of 320 to 80 W in 6 steps of 40 W each, to maintain a constant energy density of 55 J/mm³. They showed that strength and ductility of the samples decrease gradually when both laser power and laser scan speed are decreased [18].

LPBF technique leads to residual stresses that are tensile near the top and compressive near the bottom of the part. If the part is removed without caution, it will bend excessively. To avoid such displacements, a stress-relieving heat treatment may be applied. The scope of the heat treatment is to relax stresses and to reduce them, whilst fixing the part displacements. Modelling of the heat treatment has been investigated. In the current research, a beam is manufactured using PBF at five different temperatures and for six different dwell times. It is demonstrated that the displacement clearly decreases when the temperature is increased, and the ramp-up stage plays an important role in the final deflection. However, during long heat treatments at temperatures above 750 °C, the deflection increases [19]. In addition, there are studies on heat treatments that consist of more than one stage. For example, heat treatment experiments in two stages at different temperatures were carried out to verify the mechanical properties of AA 7050 [20]. For aluminium alloy 7050, other researchers investigated different durations of heat treatment to obtain a refined and homogeneous microstructure: 2 h at 420 °C and then 8 h at 470 °C before being quenched in water; and heat-treated 30 min at 470 °C, quenched in water and artificially aged at 121 °C for 16 h [21]. Moreover, the heat treatment modifies the microstructure in order to adjust the mechanical properties of a material to match its function in an application. Since SLM produces microstructures different from those of conventional manufacturing, the response to a particular heat treatment will not be similar to that of a conventionally manufactured part [22]. One parameter required for the application of a heat treatment in Simufact Additive™ is the surface heat transfer coefficient, which is the relation between the heat flux and the temperature difference. The heat transfer coefficient depends on material properties, cooling medium properties and the initial temperature and cooling time, amongst other factors [23]. For the work discussed in this paper, natural convection will be considered, with a heat transfer coefficient of $h = 5 \text{ W}/(\text{m}^2 \cdot \text{K})$ as constant value [24].

For critical applications that require high elongation, the HIP treatment is a reliable approach for improving ductility, and it allows the optimisation of SLM parameters [25]. HIP is used to eliminate pores in the material and to release residual stresses [26], as well as to densify materials due to the achieved degree of homogenisation of the alloy composition, although there is no

general scheme for the implementation of a HIP treatment since it depends highly on the application [27]. For powder metallurgy parts, combining high temperature and high pressure has shown advantages such as consolidation of material properties by creep and diffusion, healing of internal voids and strength improvement. The HIP cycle depends on the parameter temperature and pressure parameters as well as the dwell time. Both ramp-up and ramp-down slopes, also known as heating and cooling rates respectively, are determined by the maximum temperature and the dwell time of the treatment. The pressure is gradually increased, and when the temperature reaches its maximum, the pressure is then set to the maximum pressure [28–31]. For AA7050 powder, an HIP treatment was proposed between 250 and 260 °C at a pressure of 92 MPa [32], noting that the most common applied pressure in HIP treatment for aluminium alloy is 100 MPa [33, 34]. In general, there are no specific requirements for temperature, pressure, dwell time and heating and cooling rates, since these parameters depend on the application. In the literature, a wide range of temperatures (up to 2000 °C) are being investigated [33]. HIP units at maximum of 1 GPa have been already manufactured [35, 36], whilst heating and cooling rates up to 25 °C/min [37] and 3000 °C/min have been used respectively [28, 38]. The current research focuses on the ribs and spars as the most relevant components in the aircraft wing box. There are already investigations on ribs using AM techniques. For example, a rib is proposed using a specific technique known as wire arc additive manufacturing (WAAM), which manufactures components layer-by-layer using welding technology controlled by a CNC machine. This technique combines an electric arc as the heat source and a wire as the feedstock. The advantages of this method are in cost savings when manufacturing high value parts, and in shortened lead times and reduced waste material when compared to conventional manufacturing [39]. However, a rib with IoT capabilities that can be used in an Industry 4.0 platform for data collection and processing has not been considered. There is therefore a need to explore various ways of integrating sensory capability into manufacturing design processes to improve reliability of aircraft components. Embedding sensors within a desired location leads to the ability of an end-user to monitor parameters such as high temperature and pressure in specific critical regions.

This paper examines new process design solutions for wing ribs considering AM focusing on the stress and displacement requirements. The purpose is to answer the following research questions: *How does the wing rib design with a sensory embedded capability influence the AM process? What is the effect of HIP compared to normal heat treatment on the properties of AA7050–T7451 when manufacturing an aircraft wing rib?*

The Simufact Additive™ software is based on the finite element method (FEM) and has been used in this work to examine the manufacturing process for wing ribs to assess the displacements and the stresses. In this article, the SLM technique was used within PBF in AM. Details are presented in the “Results and discussion” section.

This work is structured into the following sections: “Introduction”, “Materials and methods”, “Results and discussion”, “Conclusions and further work”, and References.

2 Materials and methods

The simulation of the AM process for the wing rib was carried out in Simufact Additive™ 2021. The AM technique used to generate samples in this paper includes PBF (SLM process) since it is the most appropriate process for the fabrication of aluminium parts in the aerospace industry.

Simufact Additive™ is a piece of commercial software developed especially for PBF AM simulations. It allows the analysis of four techniques: SLM, electron beam melting (EBM), laser beam melting (LBM) and direct metal laser sintering (DMLS). It has the advantage of providing the necessary functionality to simulate the entire AM process: printing, support cutting, heat treatment, hot isostatic pressing and the evaluation of residual stresses and distortions. The voxel mesh created by Simufact Additive™ is only offered as hexahedral element and once this mesh has been created, a volumetric structure can be built, providing a 3D network. Finally, a surface mesh is generated, noting that both the voxel and surface meshes complement each other to guarantee that the whole part is covered.

Before simulating the manufacturing process for complex aircraft components using the wing rib as an example, a generic manufacturing process framework for these groups of components is designed that represents the stages the part goes through. The flowchart for this process is shown in Fig. 1.

2.1 Machine geometry

A maximum laser speed of 200 mm/s was selected that this is within the optimal range of 175–225 mm/s, with a maximum laser power of 200 W. These two parameters will be set for the simulations considering the above literature review section. The following machine parameters were used as input to set up the simulation (Table 1).

2.2 Part selection

The part was imported as a.stp file from Catia®. The relative material density was used as the initial relative density during the HIP treatment stage densification. The properties are shown in Table 2.

2.3 Support generation (Fig. 2)

The support structure method for the sensory covers was selected to be the default “Simufact” with support radius of 0.5 mm, whilst the support structure method for the wing rib was classified as

Fig. 1 Design methodology for complex aircraft components

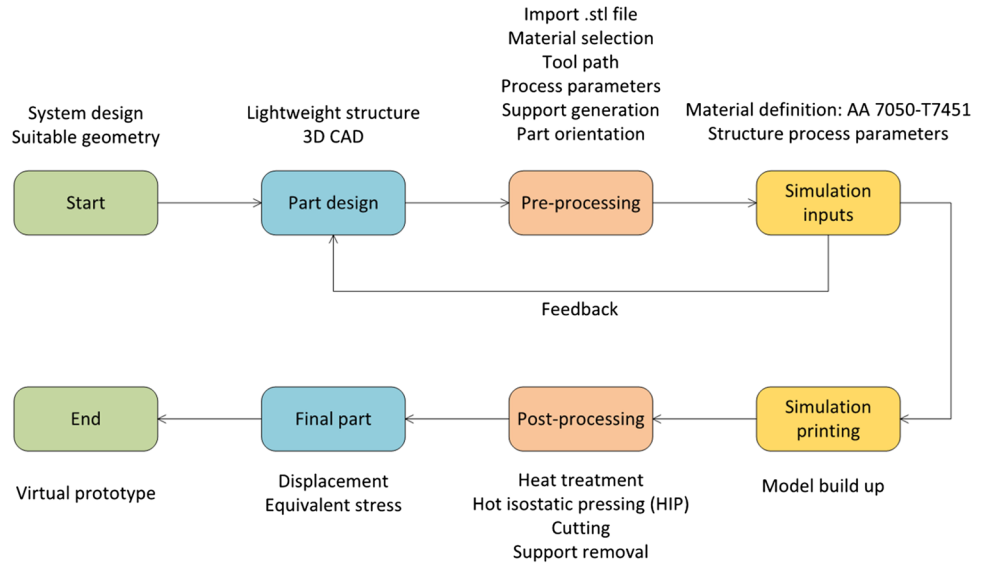


Table 1 Machine parameters

Build space dimension wing rib (mm)	X: 1100, Y: 300, Z: 300
Build space dimension sensory cover (mm)	X: 250, Y: 250, Z: 150
Corner radius base plate (mm)	24
Number of lasers	1
Max. laser power (W)	200
Max. laser speed (mm/s)	200

“Materialise” that generates block supports in this case. For the wing rib (Fig. 3), two different types of support structures were defined: one in the region near the trailing edge due to the narrowness of the geometry, and the other one corresponding to the rest of the rib. A detailed view is shown in Fig. 4.

2.4 Material selection

The mechanical properties of the aluminium alloy Al 7050-T7451 powder were introduced into Simufact Additive™ manually in order to perform the simulations (Table 3) [40].

Simufact Additive™ also required the chemical composition of the selected material, and that is presented in Table 4 [40]. The fixed value data were selected according to the corresponding composition for aluminium alloy powder.

Table 2 Part properties

Mechanical properties	Relative material density (%)	99	
	Elastic properties	Isotropic	
Thermal properties	Thermal conductivity	Isotropic	
Geometry information		Sensory cover	Wing rib
(Imported as step file from Catia)	Dimension (mm)	x: 34.7, y: 34.7, z: 12.55	x: 1000, y: 180, z: 6
	Volume	1.5772 cm ³	225.562 cm ³
	Mass	4.4188 g	631.958 g

2.5 Base plate (Table 5)

The dimensions for the base plate were chosen so that the wing rib could fit inside it.

2.6 Manufacturing parameters

The following stages for manufacturing the rib and the covers are to be investigated: build, heat treatment, HIP, cutting and support removal.

2.6.1 Build properties

For the building up process, the layer thickness 0.08 mm was considered in this work. A voxel mesh size of 2.5 mm was selected when considering the practicalities of the available computational performance. The calibration of the AA7050-T7451 with a voxel mesh size of 2.5 mm resulted in the following inherent strains: $\epsilon_{xx} = -0.0250674$, $\epsilon_{yy} = -0.02363530$, $\epsilon_{zz} = -0.03$.

2.6.2 Heat treatment

To relieve stress and to reduce displacements after cutting a heat treatment procedure are required. After applying a

Fig. 2 Sensory location with support structure

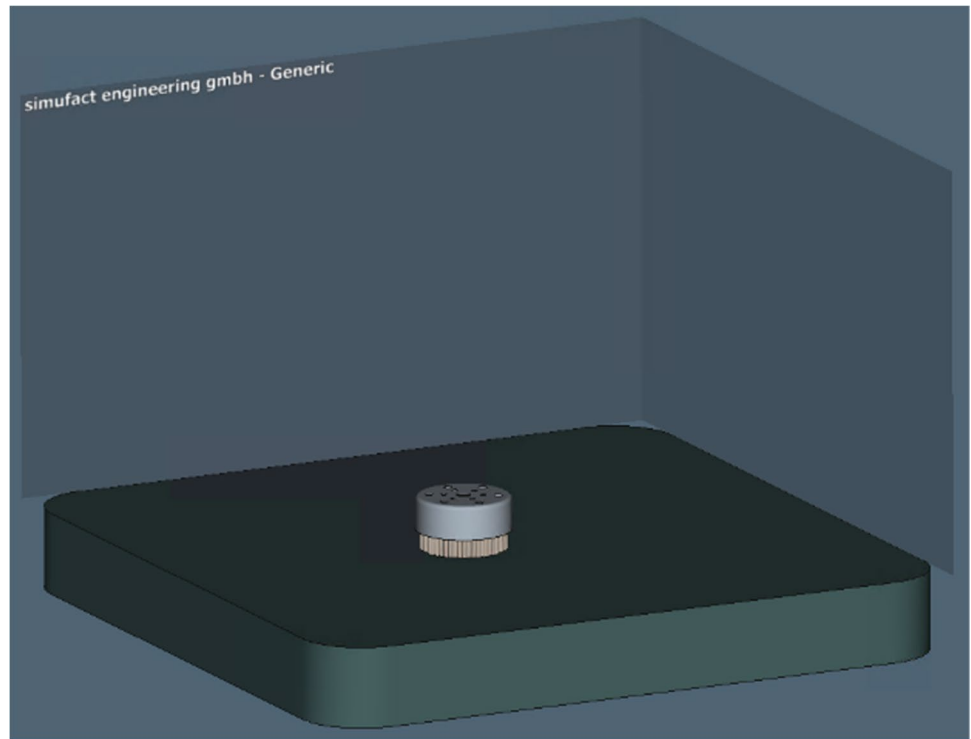


Fig. 3 Wing rib with support structure

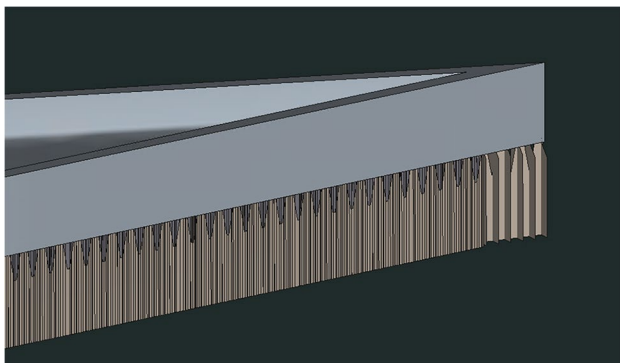
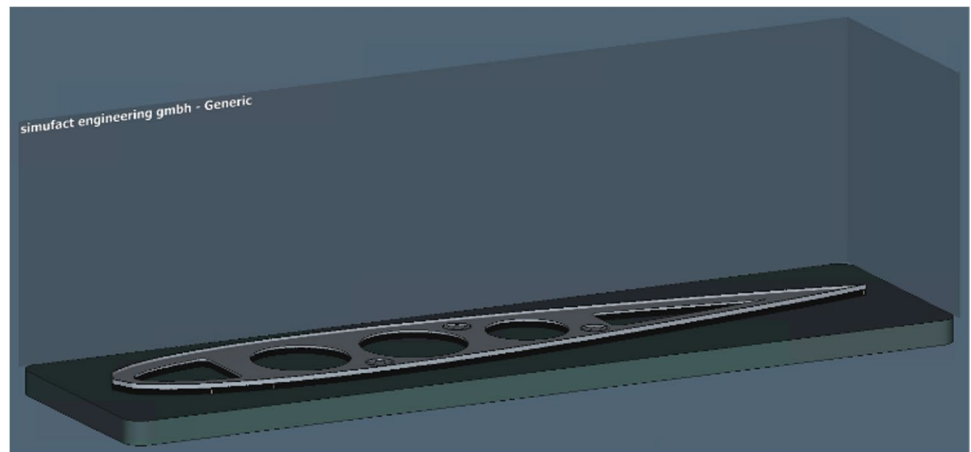


Fig. 4 Details of the wing rib support structure

conventional heat treatment process, the resulted maximum displacement from the simulations of the wing rib showed high deflections with values between 5 and 8 mm, considering different sets of ramp-up and ramp-down slopes, dwell times and maximum temperatures. The details are presented in the “[Model analysis](#)” section. Therefore, HIP was investigated and it was applied to this wing rib manufacturing process. Generally, HIP processes are represented by the showed sequence in Fig. 5. The first stage begins with an initial minimum temperature (T_{\min}) that is increased progressively up to a maximum temperature (T_{\max}) which is maintained for a certain time (t_{dwell}), and finally the temperature is decreased until the minimum desired temperature. The

Table 3 Properties for AA7050-T7451 powder

	Parameter	Value
General properties	Temperature	300–450 °C
	Effective plastic strain	0.0–0.7
	Strain rate	0.001–1.0 1/s
Powder characterisation	Average grain size	0.1 mm
	Grain size nominal range	0.05–0.2 mm
	Cold spot temperature	570 °C
	Hot spot temperature	890 °C
	Thermal properties	Thermal conductivity
	Specific heat capacity	0.86 J/(g•K)
	Density	2830 kg/m ³
	Dissipation factor	0.9
	Solidus temperature	488 °C
	Melting temperature	629 °C
Mechanical properties	Young's modulus	2.8 • e ⁴ MPa
	Poisson's ratio	0.33
	Thermal expansion coefficient	2.4 • e ⁻⁵ 1/K
	Yield strength	480 MPa
	Tensile strength	524 MPa
Electromagnetic properties	Electrical resistivity	4.2 • e ⁻⁸ Ω • m
	Electrical conductivity	2.32558 • e ⁷ 1/Ω•m

Table 4 Chemical composition of AA7050-T7451 powder (percentage mass proportion)

Element	Minimum	Maximum	Fixed value
Al	87.3	90.3	87.85
Cr	0	0.03	0.263
Cu	1	2.6	1.64
Fe	0	0.2	0.19
Mg	1.9	0.6	2.48
Mn	0	0.1	0.053
Si	0	1	0.727
Ti	0	0.1	0.095
Zn	5.7	6.7	6.52
Zr	0.08	0.2	0.018

Table 5 Base plate dimensions (mm)

	Thickness	X	Y
Sensory cover	30	250	250
Wing rib	30	1100	300

pressure is also increased from a minimum value, in this case room pressure, up to the pressure P_{HIP} which is maintained for the considered time t_{dwell} .

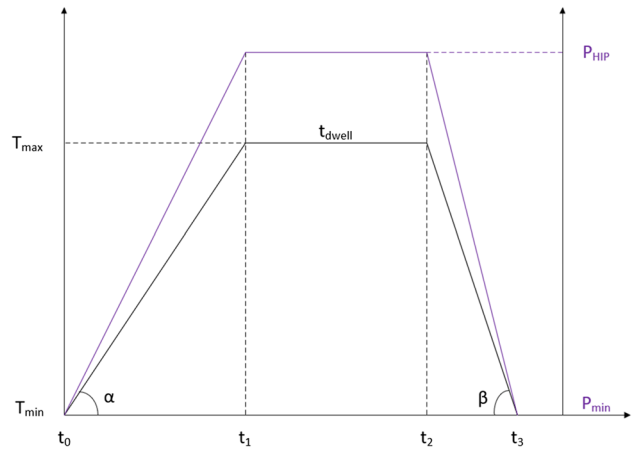


Fig. 5 Hot isostatic pressing process treatment

Table 6 Times and temperature for the heat treatment process design

Time	Temperature
t_0	$T_0 = T_{min}$
$t_1 = t_0 + \frac{T_{max} - T_{min}}{\text{Slope}_{rampup}}$	$T_1 = T_{max}$
$t_2 = t_1 + t_{dwell}$	$T_2 = T_{max}$
$t_3 = t_2 + \frac{T_{max} - T_{min}}{\text{Slope}_{rampdown}}$	$T_3 = T_{min}$

Table 7 Voxel mesh properties

	Sensory cover	Wing rib
Voxel size (mm)	2.5	2.5
Mesh type	Uniform	Uniform
Levels of coarsening	0	0
Σ voxels	1528	32,419
Σ nodes	2483	50,570
Σ layers	8	5

To design a heat treatment process, it is necessary to select the heating, dwell and cooling times. For that, the slopes

for the ramp-up and ramp-down stages will be calculated. According to Fig. 5, these slopes can be determined as follows:

$$\text{Slope}_{\text{ramp up}} = \tan\alpha = \frac{\sin\alpha}{\cos\alpha} = \frac{T_{\max} - T_{\min}}{t_1 - t_0} \quad (1)$$

$$\text{Slope}_{\text{ramp down}} = \tan\beta = \frac{\sin\beta}{\cos\beta} = \frac{T_{\max} - T_{\min}}{t_3 - t_2} \quad (2)$$

Knowing the slopes, it is possible to calculate the needed time to reach T_{\max} (t_1) and the required time to cool down to T_{\min} (t_3):

Fig. 6 Voxel mesh for sensory cover

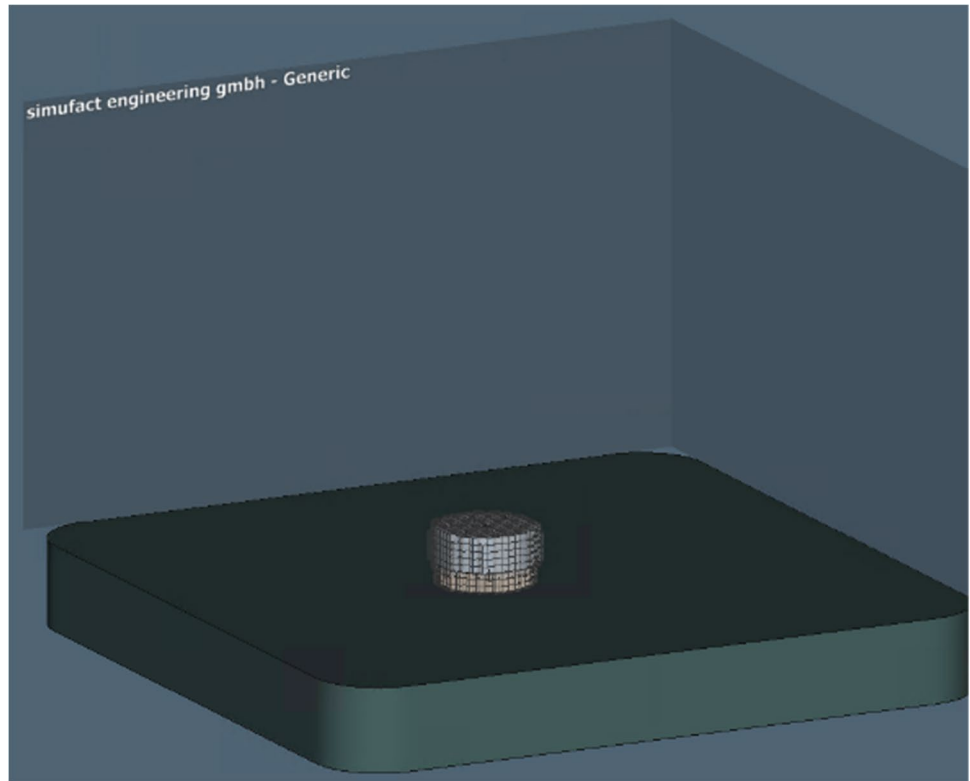
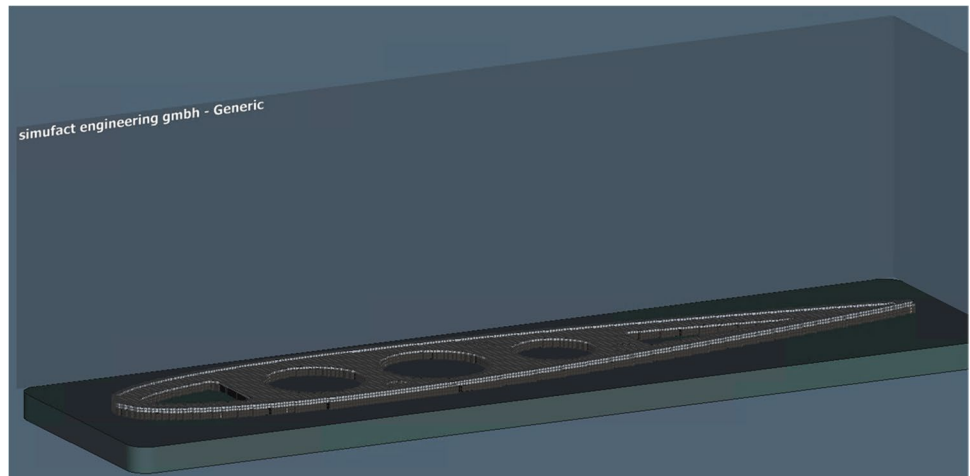


Fig. 7 Voxel mesh for wing rib



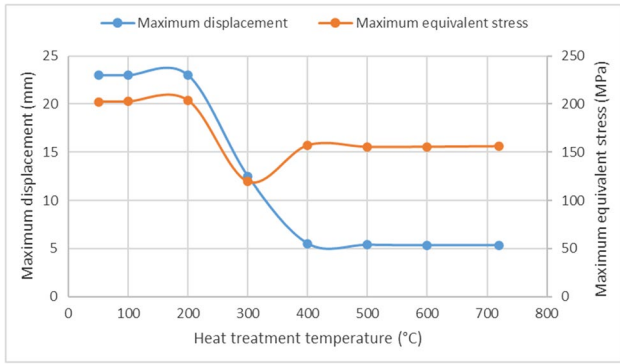


Fig. 8 Maximum displacement and maximum equivalent stress for the wing rib. Variations of T_{max} . Heating rate=1 °C/min, cooling rate=2 °C/min, t_{dwell} = 10 min

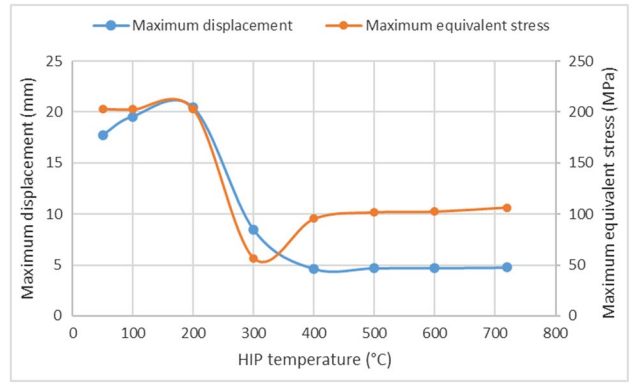


Fig. 10 Maximum displacement and maximum equivalent stress for the wing rib. Variations of T_{max} . Heating rate=1 °C/min, cooling rate=2 °C/min, t_{dwell} = 10 min, P_{HIP} = 100 MPa

$$t_1 = t_0 + \frac{T_{max} - T_{min}}{Slope_{ramp\ up}} \quad (3)$$

$$t_3 = t_2 + \frac{T_{max} - T_{min}}{Slope_{ramp\ down}} \quad (4)$$

Table 6 shows the times and temperatures for each phase of the heat treatment process:

2.6.3 Cutting

A directional cutting operation, in this case +Y (front to back) of 2 mm height, was selected and defined to cut off the parts and supports from the base plate. With this directional cutting mode, the parts and supports that are connected to the base plate are progressively cut off the plate in the specified cutting height and direction.

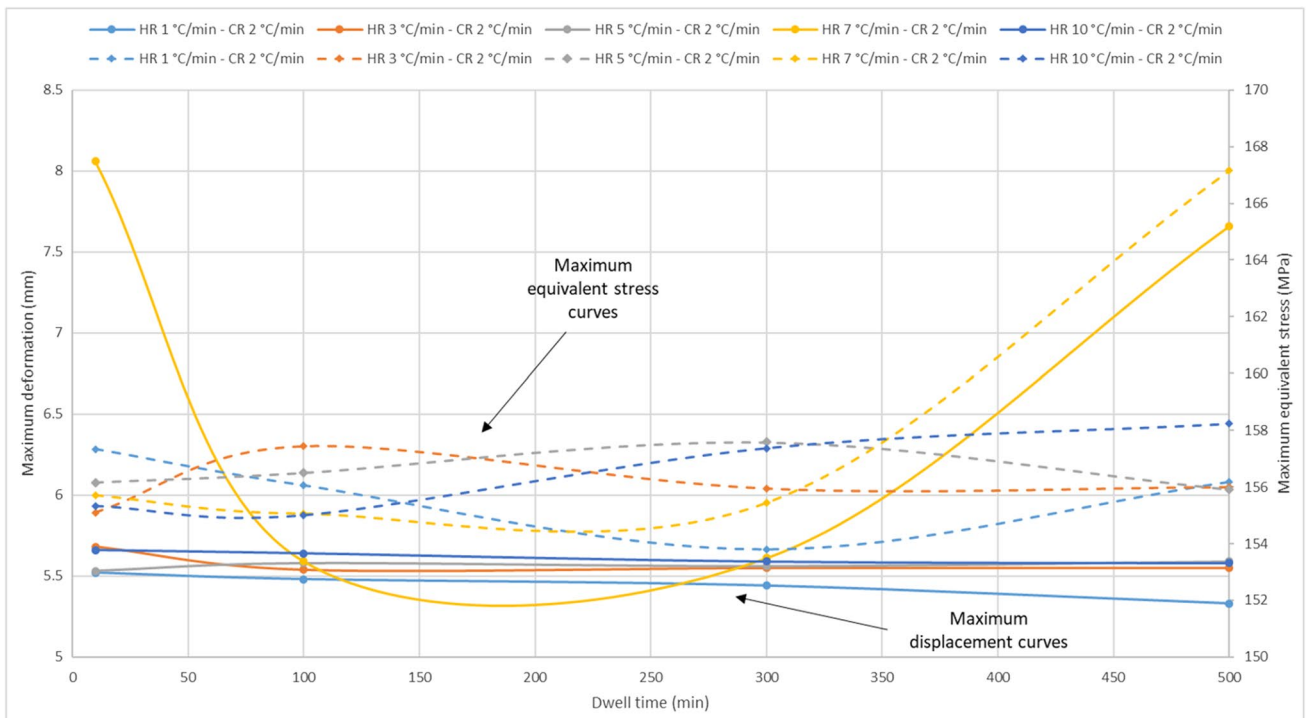


Fig. 9 Maximum displacement and maximum equivalent stress for the wing rib. Variations of heating rate and dwell time. Cooling rate=2 °C/min, T_{max} = 400 °C (— maximum displacement, - - maximum equivalent stress)

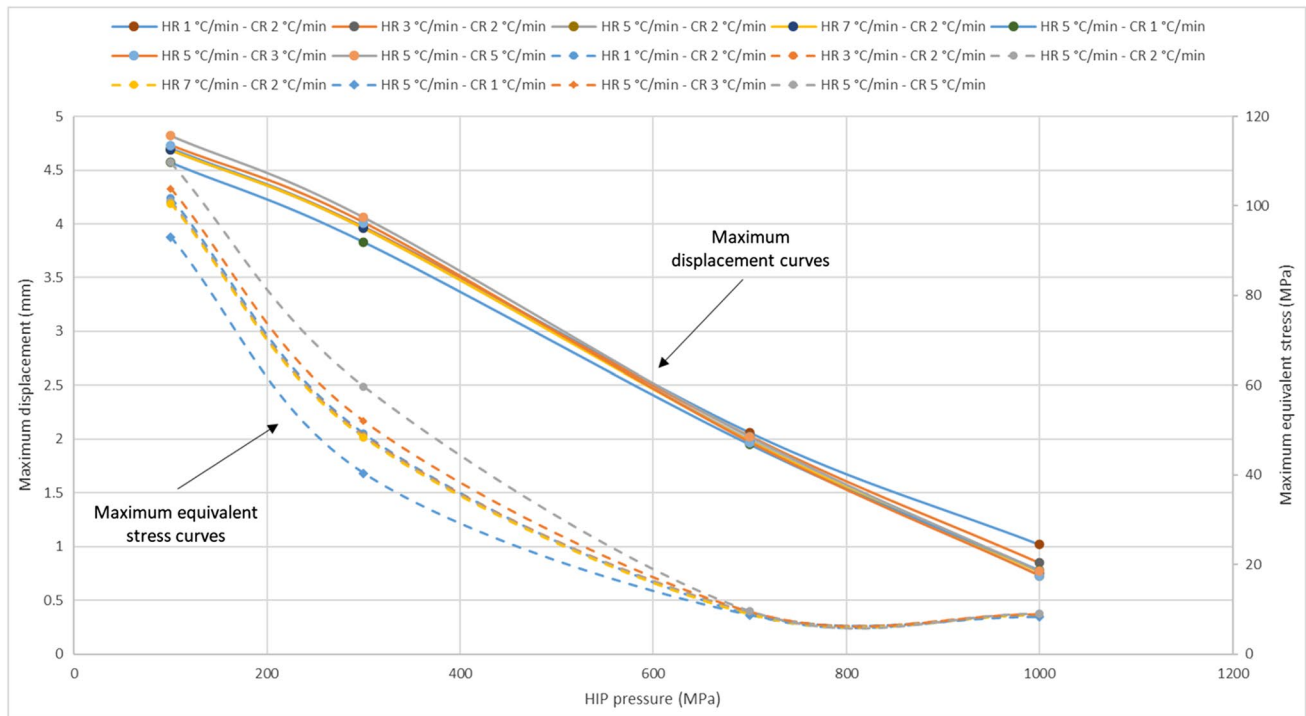


Fig. 11 Maximum displacement and maximum equivalent stress for the wing rib. Variations of heating and cooling rates, dwell time and P_{HIP} . $T_{max} = 500\text{ }^{\circ}\text{C}$ (—maximum displacement, - - maximum equivalent stress)

2.6.4 Support removal

At this stage, the support structure assigned for the wing rib was removed from the part, which resulted in the part relaxation.

2.7 Meshing and numerical parameters

Simufact Additive™ uses hexahedral elements, known as voxel elements, where parts and supports share common nodes. The mesh for the parts can be created as “Uniform”, means using the same voxel size in the X, Y and Z directions. The voxel mesh size is set to 2.5 mm. The number of voxels, nodes and layers is shown in Table 7.

The voxel meshes for the parts are shown in Figs. 6 and 7.

3 Model analysis

3.1 Wing rib with embedded sensory capability

The first analysis was the application of a conventional heat treatment process in Simufact Additive™ to relieve the stress and to reduce the displacement of the wing rib. The following set of parameters was used: heating rate = 1 °C/min, cooling rate = 2 °C/min, dwell time = 10 min and T_{max} from 50 to 720 °C. 720 °C is the maximum temperature that can be simulated according to the previously introduced

flow curves in Simufact Additive™. The results show that the maximum displacement remains almost unchanged from 400 °C, for which the value is around 5.4 mm. The same is obtained for the maximum equivalent stress with a value of approximately 155 MPa (Fig. 8).

Since the displacement was high, another set of simulations was performed with the following parameter variations: heating rate from 1 to 10 °C/min, cooling rate = 2 °C/min, dwell time from 10 to 500 min and $T_{max} = 400\text{ }^{\circ}\text{C}$. The maximum displacement is between 5.3 and 5.7 mm for all variations of the ramp-up slope apart from the case of 7 °C/

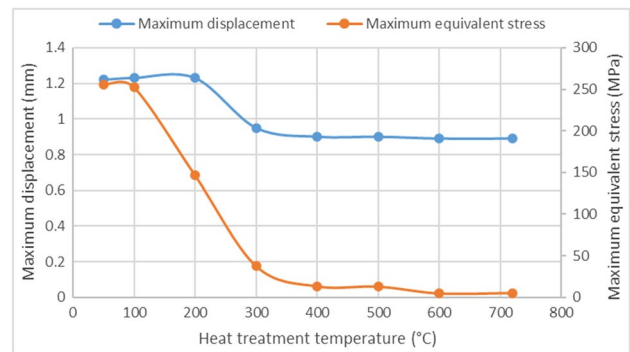


Fig. 12 Maximum displacement and maximum equivalent stress for the cover. Variations of T_{max} . Heating rate = 1 °C/min, cooling rate = 2 °C/min, $t_{dwell} = 10\text{ min}$

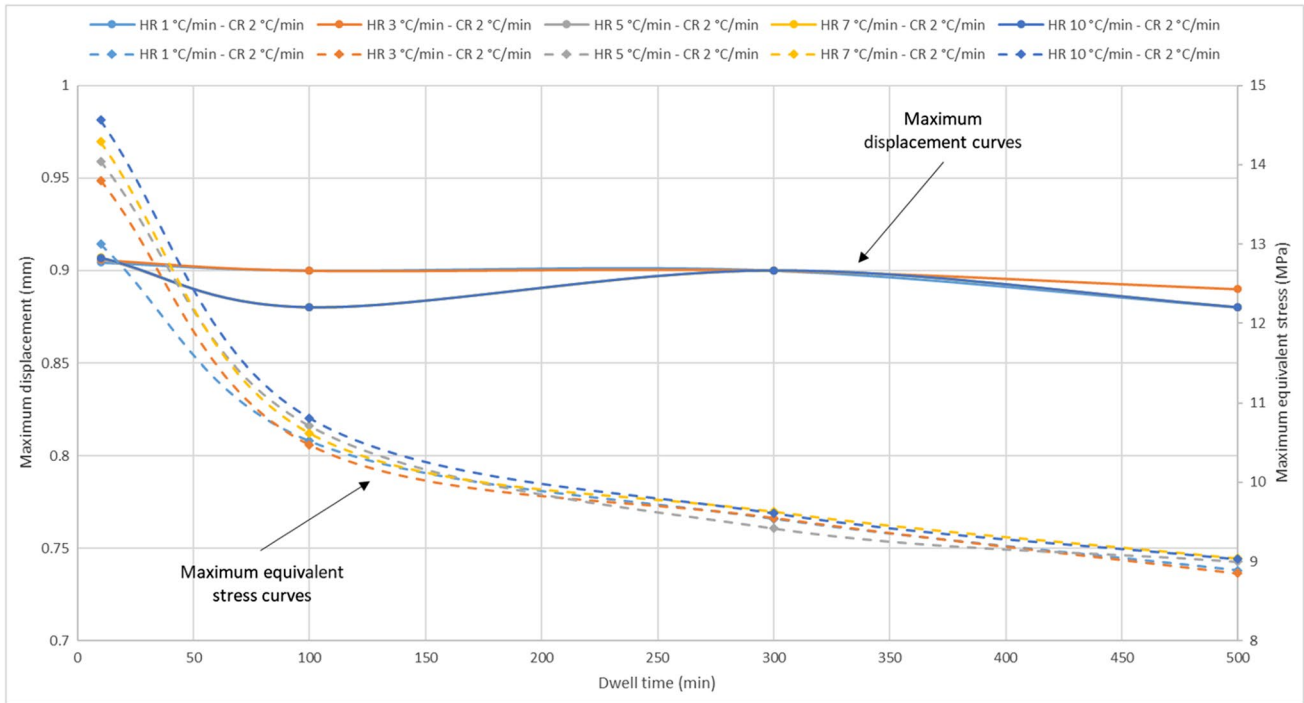


Fig. 13 Maximum displacement and maximum equivalent stress for cover. Variations of heating rate and dwell time. Cooling rate=2 °C/min, T_{max} =400 °C (— maximum displacement, - - maximum equivalent stress)

min, which seems to be a critical heating rate that should be avoided. This displacement varies between 8.1 and 5.59 mm. Figure 9 shows the maximum displacement for all cases.

The value of the maximum equivalent stress is within 154 MPa and 158 MPa for all variations except from the case of 7 °C/min, whose stress increases rapidly from a dwell time of 300 min. Since the displacement is still high, the HIP process with a maximum pressure of 100 MPa was applied for further simulations (Fig. 10). The results show that the maximum displacement remains almost unchanged from 500 °C, for which the value was 4.7 mm.

Since the displacement was still high, another set of simulations was performed with the following parameter variations: heating rate from 1 to 7 °C/min, cooling rate =2 °C/min, dwell time from 10 to 500 min, P_{HIP} from 100 to 1000 MPa and T_{max} = 500 °C (Fig. 11).

The results show that displacement and stress are highly dependent on the HIP pressure. Besides, the other parameters play an important role when designing the process. Displacement values of 1 mm or below are only obtained at P_{HIP} = 1000 MPa. The maximum equivalent stress also depends on the above parameters, but its value is always under the tensile ultimate strength of the AA7050-T7451 material (524 MPa). The optimal process was found for a heating rate of 5 °C/min, cooling rate of 3 °C/min, t_{dwell} = 10 min and T_{max} = 500 °C, whose maximum

displacement is 0.73 mm and the maximum equivalent stress is 8.9 MPa. Compared to a conventional heat treatment process, in which the maximum displacement for the wing rib was 5.4 mm, the HIP process can achieve a reduction of maximum displacement of 86.5%.

3.2 Covers for embedded sensory capability

For the covers, the first analysis was also the application of a conventional heat treatment process. The simulations were

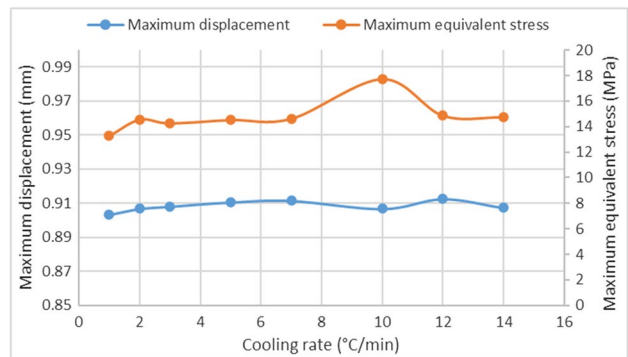


Fig. 14 Maximum displacement and maximum equivalent stress of the cover. Variations of cooling rate. T_{max} =400 °C, heating rate = 10 °C/min, t_{dwell} = 10 min

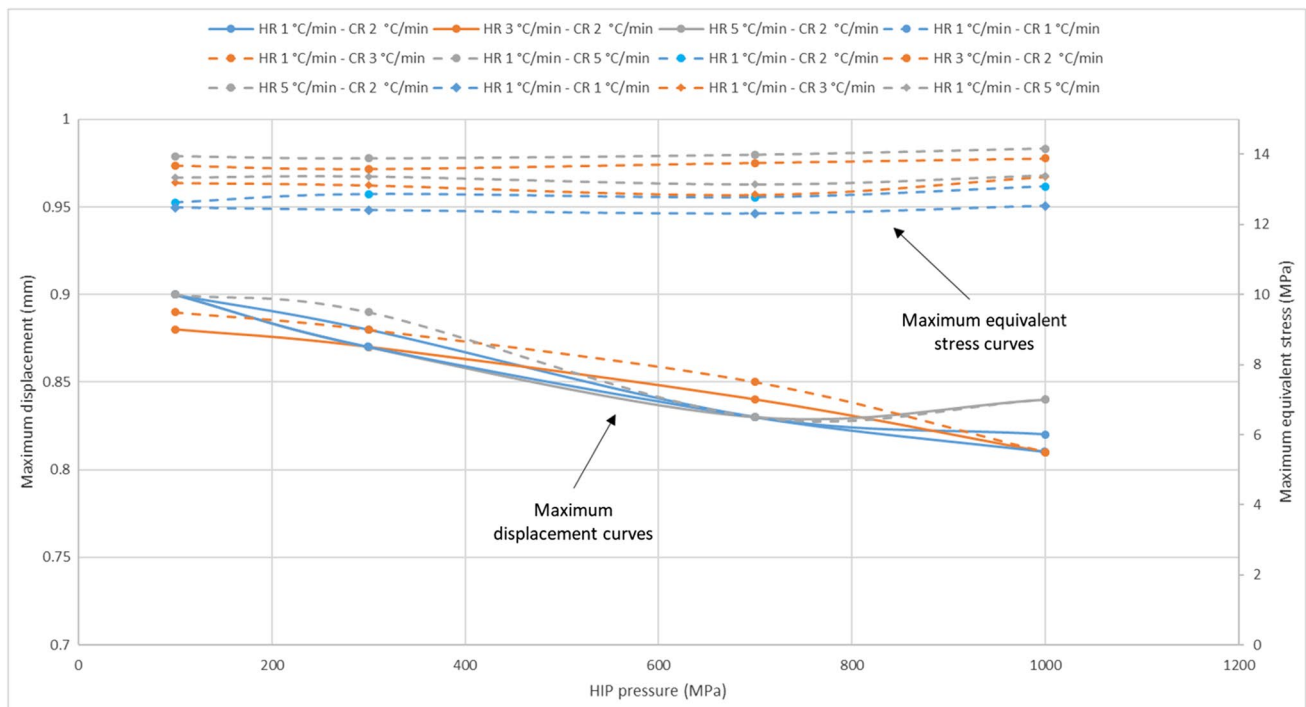


Fig. 15 Maximum displacement and maximum equivalent stress for the cover. Variations of heating and cooling rates, P_{HIP} , $T_{max} = 400\text{ }^{\circ}\text{C}$, $t_{dwell} = 10\text{ min}$ (— maximum displacement, - - maximum equivalent stress)

performed for just one cover since they are exactly the same. The following set of parameters was used: heating rate = $1\text{ }^{\circ}\text{C}/\text{min}$, cooling rate = $2\text{ }^{\circ}\text{C}/\text{min}$, dwell time = 10 min and T_{max} from 50 to $720\text{ }^{\circ}\text{C}$ (Fig. 12). $720\text{ }^{\circ}\text{C}$ is the maximum temperature that can be simulated according to the previously introduced flow curves in Simufact Additive™. The results show that the maximum displacement remains at around 0.9 mm from $400\text{ }^{\circ}\text{C}$. The maximum equivalent stress is 13 MPa at $400\text{ }^{\circ}\text{C}$ and it decreases progressively to 5.04 MPa.

Another set of simulations was performed with the following parameter variations: heating rate from 1 to $10\text{ }^{\circ}\text{C}/\text{min}$, cooling rate = $2\text{ }^{\circ}\text{C}/\text{min}$, dwell time from 10 to 500 min and $T_{max} = 400\text{ }^{\circ}\text{C}$. The maximum displacement is between 0.88 and 0.91 mm for all variations of the heating rate. The value of the maximum equivalent stress decreases progressively

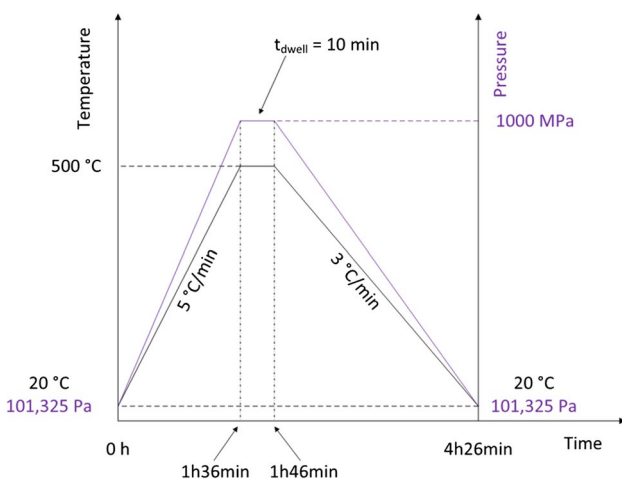


Fig. 16 HIP process for the wing rib

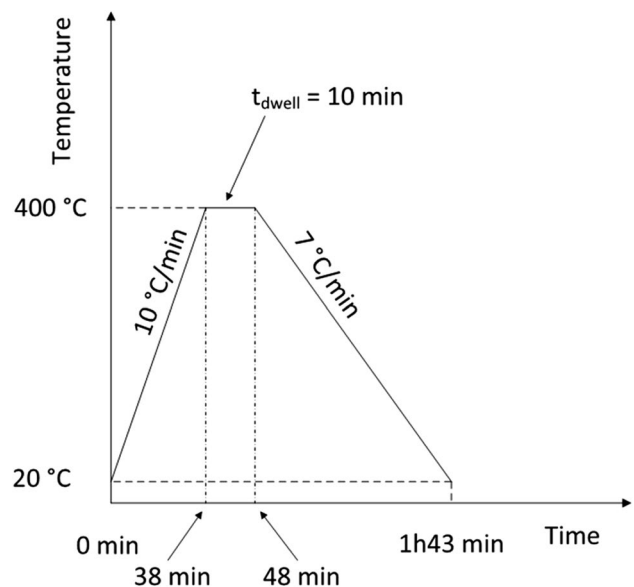


Fig. 17 Heat treatment process for the sensory cover

Table 8 Support properties

	Before support optimisation		After support optimisation		Difference	
	Volume (cm ³)	Mass	Volume (cm ³)	Mass	Volume (%)	Mass (%)
Sensory cover	8.29	18.78 g	3.92	11.10 g	-52.71	-40.89
Wing rib support 1	4515.62	10.22 kg	395.68	0.895 kg	-91.24	-91.24
Wing rib support 2 (right-hand SL)	0.311	0.704 g	0.064	0.144 g	-79.42	-79.54
Wing rib support 3 (middle SL)	0.318	0.721 g	0.063	0.144 g	-80.19	-80.03
Wing rib support 4 (left-hand SL)	0.318	0.719 g	0.063	0.144 g	-80.19	-79.97
Wing rib support 5 (trailing edge)	0.118	0.267 g	0.056	0.159 g	-52.54	-40.45

Table 9 Maximum displacement and equivalent stress for the wing rib and covers

	Sensory cover		Wing rib	
	Before support optimisation	After support optimisation	Before support optimisation	After support optimisation
Maximum displacement (mm)	0.9110	0.727	0.730	0.696
Maximum equivalent stress (MPa)	14.63	15.83	8.90	10.35

in all cases, with a value of around 9 MPa at $t_{\text{dwell}} = 500$ °C. Figure 13 shows the maximum displacement and maximum equivalent stress for all cases. The displacement does not show a high dependency on the heating rate and dwell time. Thus, the most cost-effective process is selected considering a heating rate of 10 °C/min and dwell time of 10 min.

Furthermore, for these two parameters the cooling rate was varied from 1 to 14 °C/min. The simulations show that the displacement oscillates about a constant value from a cooling rate of 7 °C/min (Fig. 14).

A HIP treatment process was also applied to the cover in order to decrease displacement and relieve stress. The outcomes of the simulations show that there is no significant influence of the HIP process compared to the conventional heat treatment: the displacement is within 0.81 and 0.9 mm. This is shown in Fig. 15.

Compared to a conventional heat treatment process, in which the maximum displacement for the cover was 0.88 mm, the HIP process can achieve a reduction in maximum displacement of 8%. The effect of the HIP on the cover is not comparable to the wing rib since their geometries are quite different. On the one hand, the wing rib has 3-mm web thickness with 6-mm upper and lower caps, and the HIP is more effective on large parts that are thin as well. On the other hand, the height of sensory cover is 12.55 mm and the HIP does not have a significant influence. Thus, a normal heat treatment is recommended due to economic reasons in terms of time and manufacturing process design.

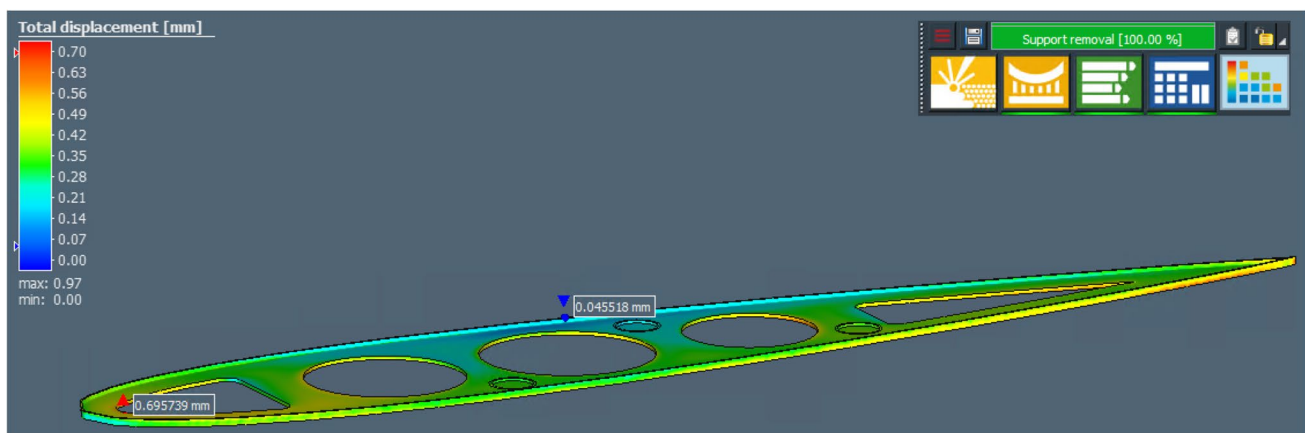


Fig. 18 Total displacement for the wing rib

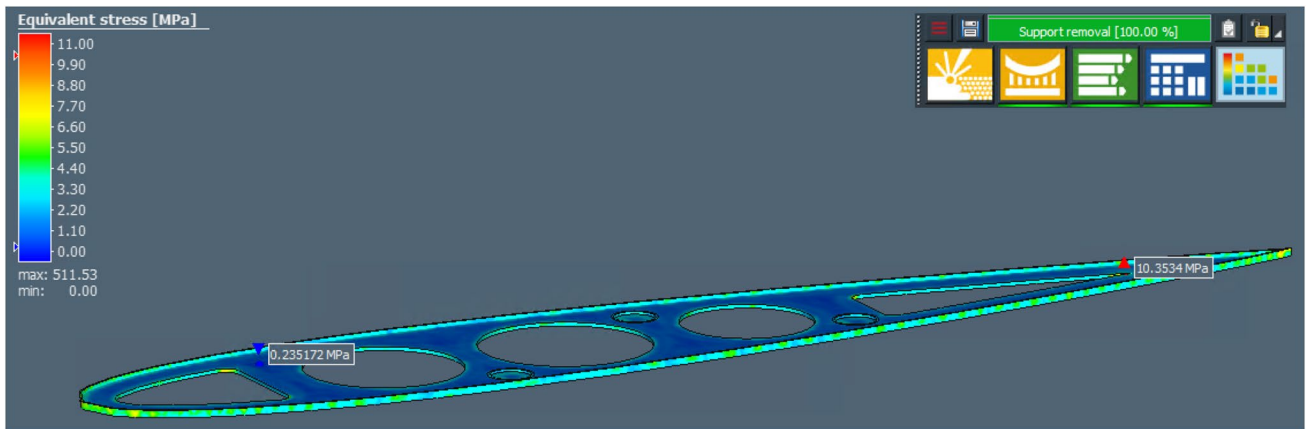


Fig. 19 Equivalent stress for the wing rib

4 Results and discussion

The outcomes of the above research show that the maximum displacement and maximum equivalent stress after a conventional heat treatment process still remain high for the wing rib. Therefore, a HIP process was applied to reduce the displacements and relieve stresses, and a reduction in maximum

displacement of 86.5% was achieved. For the cover’s manufacturing process, the HIP treatment did not show any significant influence on the displacement and the stress: though for the HIP process there is a reduction of 8% in the maximum displacement. In this case, the cost-effective manufacturing process for the covers remains the conventional heat treatment. For both parts, sets of simulations were carried out by varying the

Fig. 20 Total displacement for the cover

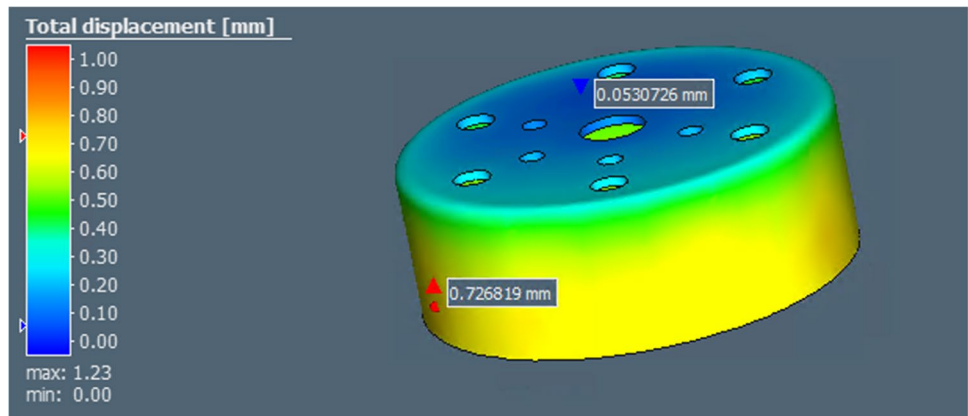
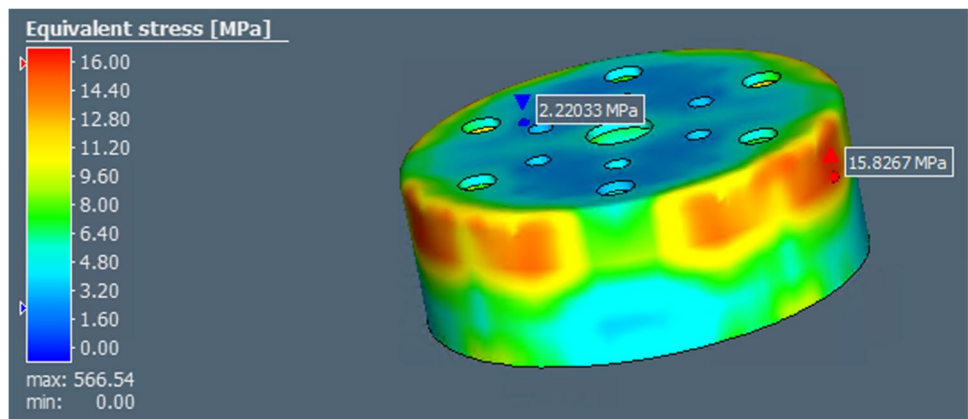


Fig. 21 Equivalent stress for the cover



heating and cooling rates, dwell time, maximum temperature of the heat treatment and maximum pressure of the HIP.

Figures 16 and 17 show the designed heat treatment processes for the wing rib and the covers.

In order to reduce costs, a support optimisation was investigated in Simufact Additive™ for the covers and the wing rib. After the support optimisation, the mass of the main wing rib support was significantly reduced by 91.24%: from 10.22 to 0.895 kg. The other supports for the sensory locations on the wing rib reduced their mass significantly by around 52% and 80%. For the covers, the mass was reduced by 40.89%. Table 8 shows an overview of the support properties before and after the support optimisation.

Considering the support optimisation, the previous designed HIP process (Fig. 16) and the conventional heat treatment (Fig. 17) were applied to the wing rib and covers, respectively. The simulations led to the following results (Table 9).

For the sensory cover, the maximum displacement was reduced by 20.20% and the maximum equivalent stress was increased by 7.58% as a result of the support optimisation. In the wing rib case, the maximum displacement decreased by 4.66% whilst the maximum equivalent stress increased by 14%.

After the support optimisation, the maximum total displacement for the wing rib is located on the leading edge, as shown in Fig. 18, whilst the maximum equivalent stress is on the trailing edge, as clarified in Fig. 19.

The simulations of the covers result in a maximum displacement and equivalent stress located on the outer surface of the cover (Figs. 20 and 21).

The convergence of the simulation was checked considering the point for which the displacement is maximum (Fig. 22). The displacement reaches a constant value after around 18,000 s of CPU time. The value of the maximum equivalent stress is also reached after this time. The convergence analysis for the sensory cover shows that the displacement reaches a constant value after around 7000 s of CPU time, whilst the value of the maximum equivalent stress was reached after around 10,000 s of CPU time (Fig. 23).

The manufacturing time was estimated by Simufact Additive™ in 31 h for the wing rib and 3 h for the sensory cover. These times were confirmed by a company that provided a quotation for printing small-scaled parts in aluminium. This company is a 3D-printing supplier based in Spain and provided 23.5 manufacturing hour for the wing rib and 30 min for the sensory cover. Due to the reduced dimensions, a HIP for the wing rib, which lasts

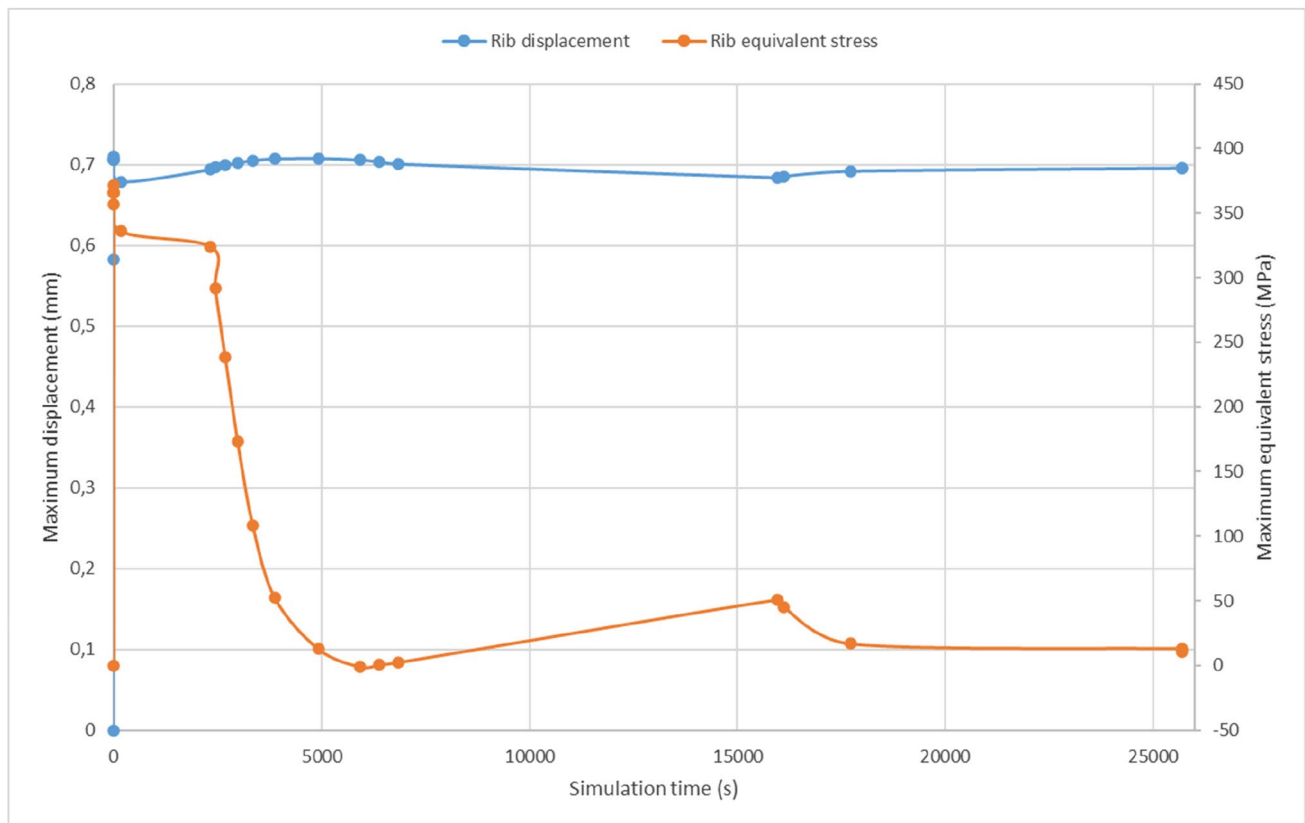


Fig. 22 Simulation convergence for the wing rib

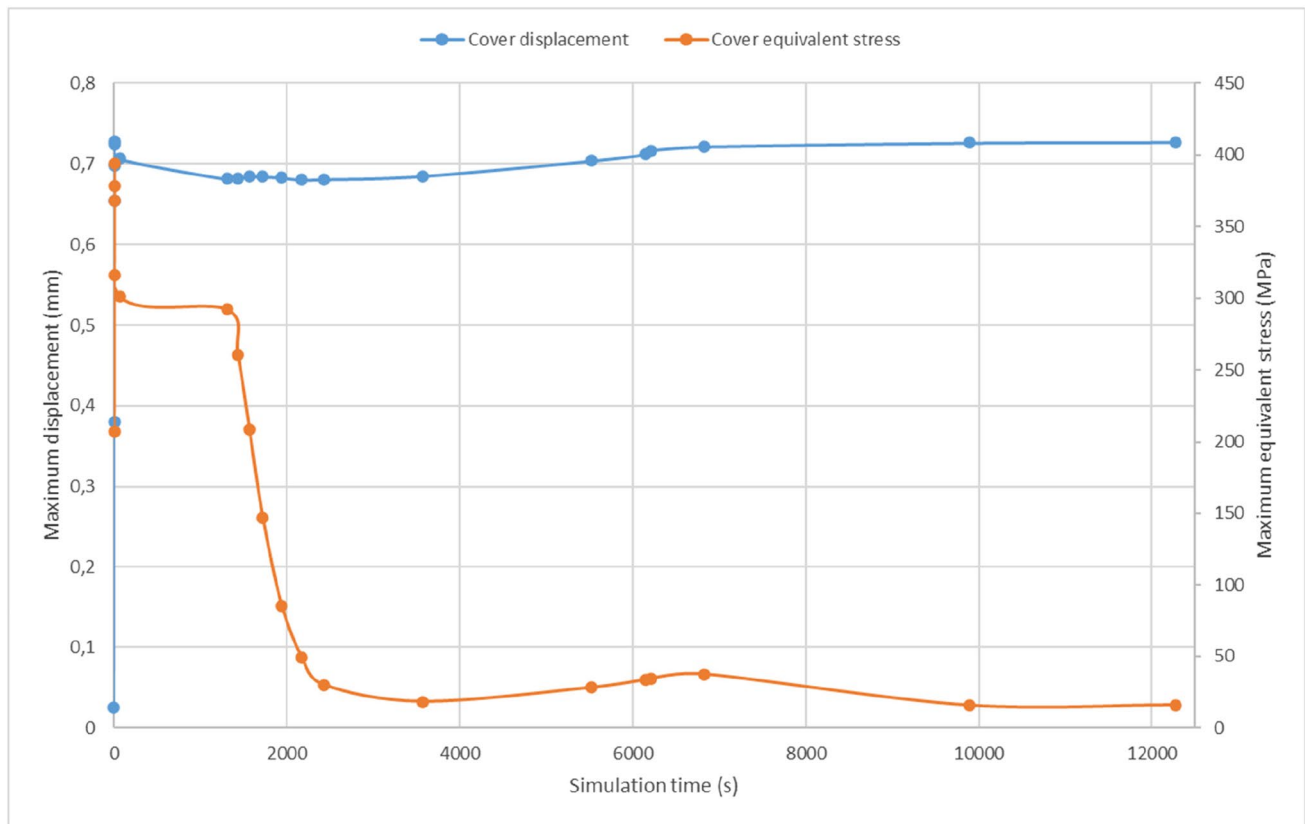


Fig. 23 Simulation convergence for the sensory cover

4.5 h in Simufact Additive™, was not necessary. In addition, the heat treatment of 2.5 h for the sensory cover was not considered.

5 Conclusions and future work

The scope of this work was to redesign the manufacturing process for wing ribs by considering embedded sensory capabilities and AM technologies. In order to design an optimal and cost-effective manufacturing process, a heat treatment procedure was investigated and proposed by varying the cooling and heating rates, the dwell time, the maximum temperature of the heat treatment and the maximum pressure of the hot isostatic pressing process. For the wing rib, the conventional heat treatment did not allow a significant reduction of displacement and stress, whilst the HIP process achieved a significant reduction of maximum displacement. For the covers, a conventional heat treatment process was selected since the HIP did not bring much improvement in displacement and stress. In addition, the support structure for both the wing rib and the covers was optimised. The results showed a significant mass and volume reduction: the mass and the volume of the main rib support were reduced by 91.24%, whilst the support of the

sensory cover achieved a reduction by 52.71% in mass and 40.89% in volume. Besides, the maximum displacement of both sensory cover and rib was reduced after support optimisation: 20.20% and 4.66% respectively.

Further work will deal with the implementation of the IoT capability into a wing rib structure manufactured using rapid prototyping for academic purposes. Recommendations can be further investigated by combining more than one thermal cycle considering different heating and cooling rates, dwell times, heat treatment temperatures and pressure variations. In addition, the thermal profile (treatment cycles) could be designed considering first the HIP process instead of a conventional heat treatment.

Acknowledgements The authors acknowledge the support of the University of Strathclyde, UK.

Author contribution Conceptualization, R. Dogea; methodology, R. Dogea; software, R. Dogea; validation, R. Dogea; formal analysis, X. T. Yan, R. Millar and R. Dogea; investigation, R. Dogea; resources, R. Dogea; data curation, R. Dogea; writing—original draft preparation, R. Dogea; writing—review and editing, X. T. Yan and R. Millar; visualisation, X. T. Yan and R. Millar; supervision, X. T. Yan and R. Millar; project administration, R. Dogea; funding acquisition, R. Dogea. All authors have read and agreed to the published version of the manuscript.

Funding This research was supported by the University of Strathclyde (Glasgow, Scotland).

Data availability All data generated or analysed during this study are included in this published article.

Code availability The code is available by request.

Declarations

Ethics approval Not applicable.

Consent to participate Not applicable.

Conflict of interest The authors declare no competing interests.

Open Access This article is licensed under a Creative Commons Attribution 4.0 International License, which permits use, sharing, adaptation, distribution and reproduction in any medium or format, as long as you give appropriate credit to the original author(s) and the source, provide a link to the Creative Commons licence, and indicate if changes were made. The images or other third party material in this article are included in the article's Creative Commons licence, unless indicated otherwise in a credit line to the material. If material is not included in the article's Creative Commons licence and your intended use is not permitted by statutory regulation or exceeds the permitted use, you will need to obtain permission directly from the copyright holder. To view a copy of this licence, visit <http://creativecommons.org/licenses/by/4.0/>.

References

1. Arrizubieta JI, Ukar O, Ostolaza M, Mugica A (2020) Study of the environmental implications of using metal powder in additive manufacturing and its handling. *Metals* (Basel) 10(2):261. <https://doi.org/10.3390/met10020261>
2. Adeyemi A, Akinlabi ET, Mahamood RM (2018) Powder bed based laser additive manufacturing process of stainless steel: a review, in *Materials Today: Proceedings* 5(9). <https://doi.org/10.1016/j.matpr.2018.06.193>
3. Hansen HN et al (2019) Additive manufacturing of metal components - process-material interaction in different process chains, in *IOP Conference Series: Mater Sci Eng* 580(1). <https://doi.org/10.1088/1757-899X/580/1/012006>
4. Blakey-Milner B et al (2021) Metal additive manufacturing in aerospace: a review. *Mater Des* 209. <https://doi.org/10.1016/j.matdes.2021.110008>
5. Parthasarathy J Starly B, Raman S, Christensen A (2010) Mechanical evaluation of porous titanium (Ti6Al4V) structures with electron beam melting (EBM). *J Mech Behav Biomed Mater* 3(3). <https://doi.org/10.1016/j.jmbbm.2009.10.006>
6. Meng L et al (2020) From topology optimization design to additive manufacturing: today's success and tomorrow's roadmap. *Arch Comput Methods Eng* 27(3). <https://doi.org/10.1007/s11831-019-09331-1>
7. Tepylo N, Huang X, Patnaik PC (2019) Laser-based additive manufacturing technologies for aerospace applications. *Adv Eng Mater* 21(11). <https://doi.org/10.1002/adem.201900617>
8. Rodrigue H, Rivette M (2010) An assembly-level design for additive manufacturing methodology. *IDMME-Virtual Concept*, Oct 2010, Bordeaux, France. ?10.1007/978-2-8178-0169-8?.?hal-01099485?
9. Herzog D, Seyda V, Wycisk E, Emmelmann C (2016) Additive manufacturing of metals. *Acta Mater* 117. <https://doi.org/10.1016/j.actamat.2016.07.019>
10. DIN, E. (2017). *ISO/ASTM 52900: Additive Fertigung—Grundlagen—Terminologie (ISO/ASTM 52900: 2015); Deutsche Fassung EN ISO/ASTM 52900*. <https://doi.org/10.31030/3290011>
11. Sjarov M, Ceriani N, Lechler T, Franke J (2020, September) Building blocks for digitally integrated process chains in PBF-based additive manufacturing. In: *Congress of the German academic association for production technology*. Springer, Berlin, Heidelberg, pp 368–377. https://doi.org/10.1007/978-3-662-62138-7_37
12. Thrumurthulu K, Pandey PM, Reddy NV (2004) Optimum part deposition orientation in fused deposition modeling. *Int J Mach Tools Manuf* 44(6). <https://doi.org/10.1016/j.ijmactools.2003.12.004>
13. Jiang J, Xu X, Stringer J (2018) Support structures for additive manufacturing: a review. *J Manuf Mater Process* 2(4):64. <https://doi.org/10.3390/jmmp2040064>
14. Jiang J, Xu X, Stringer J (2019) Optimisation of multi-part production in additive manufacturing for reducing support waste. *Virtual Phys Prototyp* 14(3). <https://doi.org/10.1080/17452759.2019.1585555>
15. Schelhorn L, Gosch M, Debeugny L, Schröter P, Schwarz W, Soller S (2019) Optimal design and process simulation for additive manufacturing, 8Th Eur. Conf Aeronaut Sp Sci. <https://doi.org/10.13009/EUCASS2019-354>
16. Hossain MS et al (2016) Fabrication of smart parts using powder bed fusion additive manufacturing technology. *Addit Manuf* 10:58–66. <https://doi.org/10.1016/j.addma.2016.01.001>
17. Morgan D, Agba E, Hill C (2017) Support structure development and initial results for metal powder bed fusion additive manufacturing. *Procedia Manuf* 10:819–830. <https://doi.org/10.1016/j.promfg.2017.07.083>
18. Wang Z et al (2020) Selective laser melting of aluminum and its alloys. *Materials* (Basel) 13(20):4564. <https://doi.org/10.3390/ma13204564>
19. De Baere D et al (2021) Thermo-mechanical modelling of stress relief heat treatments after laser-based powder bed fusion. *Addit Manuf* 38(October 2020):101818. <https://doi.org/10.1016/j.addma.2020.101818>
20. Zhao Y, Sargent N, Li K, Xiong W (2020) A new high-throughput method using additive manufacturing for alloy design and heat treatment optimization. *Materialia* 13(May):100835. <https://doi.org/10.1016/j.mtla.2020.100835>
21. Mazzer EM, Afonso CRM, Bolfarini C, Kiminami CS (2013) Microstructure study of Al 7050 alloy reprocessed by spray forming and hot-extrusion and aged at 121 C. *Intermetallics* 43. <https://doi.org/10.1016/j.intermet.2013.08.004>
22. Aboulkhair NT, Everitt NM, Ashcroft I, Tuck C (2014) Reducing porosity in AlSi10Mg parts processed by selective laser melting. *Addit Manuf* 1. <https://doi.org/10.1016/j.addma.2014.08.001>
23. Hou W, Ji W, Zhang Z, Xie J (2013) The surface heat transfer coefficient model of 7075 Al-alloy extrusion product and its temperature prediction. *Mater Sci Forum* 749:229–236. <https://doi.org/10.4028/www.scientific.net/MSF.749.229>
24. Fezi K, Krane MJM (2017) Influence of a wiper on transport phenomena in direct chill casting of aluminium alloy 7050. *Int J Cast Met Res* 30(4). <https://doi.org/10.1080/13640461.2017.1286552>
25. Zhou SY, Su Y, Wang H, Enz J, Ebel T, Yan M (2020) Selective laser melting additive manufacturing of 7xxx series Al-Zn-Mg-Cu alloy: cracking elimination by co-incorporation of Si and TiB₂. *Addit Manuf* 36. <https://doi.org/10.1016/j.addma.2020.101458>
26. Seabra M et al (2016) Selective laser melting (SLM) and topology optimization for lighter aerospace components, in *Procedia Structural Integrity* 1. <https://doi.org/10.1016/j.prostr.2016.02.039>

27. Mujica Roncery L, Lopez-Galilea I, Rutttert B, Huth S, Theisen W (2016) Influence of temperature, pressure, and cooling rate during hot isostatic pressing on the microstructure of an SX Ni-base superalloy. *Mater Des* 97. <https://doi.org/10.1016/j.matdes.2016.02.051>
28. Eklund A, Ahlfors M (2018) Heat treatment of PM parts by hot isostatic pressing. *Met Powder Rep* 73(3). <https://doi.org/10.1016/j.mprp.2018.01.001>
29. Yegyan Kumar A, Bai Y, Eklund A, Williams CB (2018) The effects of hot isostatic pressing on parts fabricated by binder jetting additive manufacturing. *Addit Manuf* 24. <https://doi.org/10.1016/j.addma.2018.09.021>
30. Goel S, Sittiho A, Charit I, Klement U, S Joshi (2019) Effect of post-treatments under hot isostatic pressure on microstructural characteristics of EBM-built Alloy 718. *Addit Manuf* 28. <https://doi.org/10.1016/j.addma.2019.06.002>
31. Hafenstein S, Werner E (2019) Pressure dependence of age-hardenability of aluminum cast alloys and coarsening of precipitates during hot isostatic pressing. *Mater Sci Eng A* 757. <https://doi.org/10.1016/j.msea.2019.04.077>
32. Li JL, Li SS, Xiong YC (2013) Bulk nanocrystalline Al 7050 prepared via cryomilling, in *Advanced Materials Research* 779. <https://doi.org/10.4028/www.scientific.net/AMR.779-780.34>
33. Atkinson HV, Davies S (2000) Fundamental aspects of hot isostatic pressing: an overview. *Metall Mater Trans A* 31(12):2981–3000. <https://doi.org/10.1007/s11661-000-0078-2>
34. Gushev MN, Sridharan N, Thompson Z, Terrani KA, Babu SS (2018) Influence of hot isostatic pressing on the performance of aluminum alloy fabricated by ultrasonic additive manufacturing. *Scr Mater* 145. <https://doi.org/10.1016/j.scriptamat.2017.10.004>
35. Ishihara S, Gu H, Bill J, Aldinger F, Wakai F (2002) Densification of precursor-derived Si-C-N ceramics by high-pressure hot isostatic pressing. *J Am Ceram Soc* 85(7). <https://doi.org/10.1111/j.1151-2916.2002.tb00339.x>
36. Bocanegra-Bernal MH (2004) Hot isostatic pressing (HIP) technology and its applications to metals and ceramics. *J Mater Sci* 39(21). <https://doi.org/10.1023/B:JMSC.0000044878.11441.90>
37. Sobota P et al (2020) Fabrication of Y6MoO12 molybdate ceramics: from synthesis of cubic nano-powder to sintering. *Ceram Int* 46(4). <https://doi.org/10.1016/j.ceramint.2019.10.192>
38. Weddeling A, Theisen W (2017) Energy and time saving processing: a combination of hot isostatic pressing and heat treatment. *Met Powder Rep* 72(5). <https://doi.org/10.1016/j.mprp.2016.04.001>
39. Lockett H, Ding J, Williams S, Martina F (2017) Design for wire + arc additive manufacture: design rules and build orientation selection. *J Eng Des* 28(7–9):568–598. <https://doi.org/10.1080/09544828.2017.1365826>
40. AIH Committee (1990) *ASM Handbook Vol 2-Properties and selection: Nonferrous alloys and special purpose materials*. ASM International, Materials Park. <https://doi.org/10.31399/asm.hb.v02.9781627081627>

Publisher's note Springer Nature remains neutral with regard to jurisdictional claims in published maps and institutional affiliations.